RA'EGA
O ESPAÇO GEOGRÁFICO EM ANÁLISE
https://revistas.ufpr.br/raega

ISSN eletrônico 2177-2738
RA'EGA, Curitiba, PR, V.62, n.1, p. 44–66, 4/2025
http://dx.doi.org/10.5380/raega.v62i1.98349

Spatiotemporal variability of reference evapotranspiration estimated using satellite images in the Tibagi River Basin, Paraná State, Brazil

Variabilidade espaço-temporal da evapotranspiração de referência estimada com imagens de satélites na bacia hidrográfica do rio Tibagi, estado do Paraná, Brasil

Jorge Luiz Moretti de Souza[*], **Denis Pinheiro da Silva**[**], **Daniela Jerszurki**[***]

[*]Departamento de Solos e Engenharia Agrícola, Universidade Federal do Paraná, jmoretti@ufpr.br
[**]Departamento de Solos e Engenharia Agrícola, Universidade Federal do Paraná, Silva-denispinheiro263@gmail.com
[***]NDrip Israel, Center Israel, danijerszurki@gmail.com

http://dx.doi.org/10.5380/raega.v62i1.98349

Abstract

The reference evapotranspiration (*ETo*) is an essential tool in planning and management of water resources, but large-scale monitoring using traditional methods is impractical due to its cost and logistics. An alternative is to rely on remote data to model *ETo*. This study aimed to evaluate the spatial variability of daily *ETo* in the Tibagi River Basin (TRB), estimated with remote sensing data during years with ENSO events, and to estimate *ETo* between Landsat satellite images using a temporal interpolation algorithm. *ETo* was calculated using the Moretti-Jerszurki-Silva model (*MJS*; $ETo_{MJS(\psi air;Ra)}$) and spatial data of temperature and relative humidity were estimated with a multiple linear regression model. Spatial variability was assessed using images that represented the seasons in 2013 (Normal), 2015 (El Niño), and 2011 (La Niña). The temporal variability of $ETo_{MJS(\psi air;Ra)}$ was tested with linear interpolation between Landsat 8 images in 2013, using the "r.series.interp" algorithm. The interpolated $ETo_{MJS(\psi air;Ra)int}$ was compared with ETo_{PM} calculated with the Penman-Monteith method using daily climatic data coming from local meterological stations. The spatialized *ETo* identified differences in the seasons under the analyzed climate scenarios, which was not possible with ETo_{PM}. The methodology for estimating spatialized $ETo_{MJS(\psi air;Ra)}$ over large areas showed acceptable accuracy, despite being laborious for extensive coverage. Temporal *ETo* showed satisfactory statistical accuracy ($RMSE$ = 0,65 mm dia^{-1}; r = 0,73; $MAPE$ = 5,94%; NSE = –1,2; d = 0,04), although the limitations of the images and the linear interpolation algorithm limited the monitoring of daily ETo_{PM} variations.

Keywords:
Mapping, Modeling, Climate scenarios, Land cover.

ISSN eletrônico 2177-2738
RA'EGA, Curitiba, PR, V.62, n.1, p. 44–66, 4/2025
http://dx.doi.org/10.5380/raega.v62i1.98349

Resumo

A evapotranspiração de referência (*ETo*) é essencial para planejamento e gestão dos recursos hídricos, mas monitorá-la em larga escala com métodos tradicionais é inviável devido ao custo e logística. Uma alternativa é utilizar dados obtidos remotamente para a modelagem da *ETo*. Teve-se por objetivo no presente estudo avaliar a variabilidade espacial da *ETo* diária na bacia hidrográfica do rio Tibagi (BHRT), estimada com dados remotos em anos com ocorrência de eventos ENOS, e estimar a *ETo* no intervalo entre imagens do satélite Landsat com um algoritmo interpolador temporal. A *ETo* foi calculada com o modelo Moretti-Jerszurki-Silva (*MJS*; $ETo_{MJS(\psi ar;Ra)}$) e dados espacializados de temperatura e umidade relativa do ar, estimados com modelo de regressão linear múltiplo. A variabilidade espacial foi avaliada com imagens das estações de 2013 (Normal), 2015 (El Niño) e 2011 (La Niña). A variabilidade temporal da $ETo_{MJS(\psi ar;Ra)}$ foi testada com interpolação linear entre imagens Landsat 8 de 2013, utilizando o algoritmo "r.series.interp". A $ETo_{MJS(\psi ar;Ra)int}$ interpolada foi comparada com a ETo_{PM} Penman-Monteith, calculada com dados diários de estações meteorológicas. A *ETo* espacializada identificou diferenças nas estações do ano nos cenários climáticos analisados, não observadas com a ETo_{PM}. A metodologia para estimar a $ETo_{MJS(\psi ar;Ra)}$ espacializada em grandes áreas obteve precisão aceitável, apesar do processo ser laborioso para coberturas amplas. A *ETo* temporal apresentou precisão estatística satisfatória (*RMSE* = 0,65 mm dia^{-1}; *r* = 0,73; *MAPE* = 5,94%; *NSE* = –1,2; *d* = 0,04), embora limitações das imagens e algoritmo interpolador linear dificultassem o acompanhamento das variações diárias da ETo_{PM}.

Palavras-chave:
Mapeamento, Modelagem, Cenários climáticos, Cobertura do solo.

I. INTRODUCTION

Reference evapotranspiration (*ETo*) is a fundamental component for water resource planning and management, particularly for conducting water balance analyses in river basins (ASCE-EWRI, 2005; Allen et al., 2011; Jerszurki et al., 2017). Monitoring *ETo* on a large scale using traditional methods (measurements with evapotranspirometers and lysimeters or estimates with physical or empirical models) is not feasible due to high costs, logistical challenges, lack of spatial continuity, and the requirement for local climate data (Rosa et al., 2023). An alternative is to use remotely obtained data for *ETo* modeling (Talsma et al., 2018). However, few studies validate and utilize remote sensing for *ETo* estimation. Deriving *ETo* through remote sensing can significantly contribute to studies on a regional to global scale by providing spatialized and cost-effective estimates (Paredes et al., 2021).

Climatic data are measured at weather stations, which may not be available in certain locations where evapotranspiration estimation is desired (Rosa et al., 2023). *ETo* exhibits significant spatial variability due to environmental conditions and variations (ASCE-EWRI, 2005; Paredes et al., 2021). Consequently, point-based *ETo* measurements determined by conventional methods may not represent the surrounding area, limiting the assessment of *ETo* variability. In the state of Paraná, the *Instituto Nacional de Meteorologia* (INMET) operates 25 weather stations across a territorial area of 199280 km^2. Each station represents approximately 8000 km^2 with a single *ETo* value. Beyond the spatial importance of *ETo*, studies considering the effects of the El Niño-Southern Oscillation (ENSO) phenomenon are relevant, as projections indicate that ENSO events are likely to occur with greater frequency and intensity in the coming years (Cavalcante et al., 2015).

Satellite imagery is an interesting alternative for studies aiming to estimate *ETo* for a region spatially and temporally. Modern satellite constellations (such as Planet, Satellogic, AxelSpace, among others) have reduced limitations related to spatial and temporal resolution, offering frequent (daily) and high-resolution (up to 0.5 m) images. However, challenges remain (data integration from constellations and spectral limitations for specific applications), and costs may restrict their use in research involving long-term historical analysis, which often relies on free or open-access solutions (Nagel et al., 2020).

Landsat images are free of charge but have a spatial resolution of 30 m and a temporal resolution of 16 days, which can represent challenges for daily monitoring of crop growth and development, especially under conditions of minimal or no cloud cover (Gao et al., 2006). Daily monitoring of *ETo* with high spatial and temporal resolution is essential to understanding its dynamics, providing critical information on crop water-use efficiency and soil moisture, thereby supporting the optimization of irrigation water use (Cammalleri et al., 2013; Paredes et al., 2021; Rosa et al., 2023).

The Moderate Resolution Imaging Spectroradiometer (MODIS) sensor has moderate spatial resolutions (250, 500, and 1000 meters) and daily temporal resolution. Ke et al. (2017) considered the sensor's spatial resolution to be a significant limitation for its use at local or watershed scales for irrigation purposes or water resource management. Ideally, continuous and high spatial resolution *ETo* maps should be generated. However, currently available remote sensing satellites cannot provide high spatial and temporal resolution imagery on a single platform for free, due to the trade-off that must exist between these resolutions (Wang et al., 2019).

In the literature, advanced and complex algorithms have been developed to improve the spatial resolution of Landsat imagery (Gao et al., 2006; Zhu et al., 2010) and have been utilized by several authors (Yang et al., 2016; Ke et al., 2017). However, it is believed that simplified algorithms can facilitate free access to datasets with high spatial and temporal resolution, supporting the development of technical activities and scientific studies. Moreover, more complex algorithms do not always result in lower errors compared to simpler ones. Therefore, the objective of the present study was to evaluate the spatial variability of daily reference evapotranspiration (*ETo*) in the Tibagi River Basin (TRB), estimated using remote data during years with ENSO events (El Niño, La Niña, and Neutral conditions), as well as to estimate the basin's *ETo* for the intervals between Landsat satellite images using a temporal interpolation algorithm.

II. MATERIALS AND METHODS

The study area consisted of the Tibagi River Basin (TRB), located in the central-eastern portion of the State of Paraná (Figure 1), covering approximately 13% of the state's territorial area (25000 km^2) and characterized by the Cfa and Cfb climate types (Alvares et al., 2013). The TRB was selected due to its distinct physical and climatic characteristics related to its geographical location. This physical and climatic distinction was desirable for evaluating the spatial and temporal variability of *ETo*.

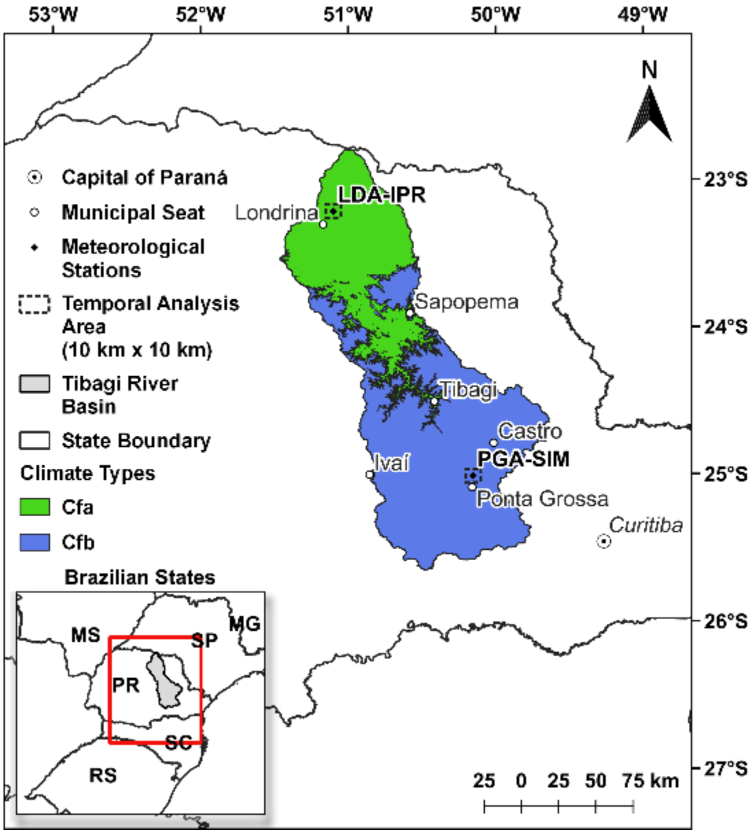

Figure 1 – Location of the Tibagi River Basin (TRB), showing the distribution of its meteorological stations and a 10 km x 10 km subset for temporal analysis (LDA-IPR and PGA-SIM). (Source: The authors)

ETo was estimated using the Moretti-Jerszurki-Silva (MJS) model (Jerszurki et al., 2017; Equations 1 to 4), which considers the atmospheric water potential (ψ_{air}) and solar radiation at the top of the atmosphere (*Ra*).

$$ETo_{MJS(\psi air;Ra)} = a + b \cdot Ee_i \tag{1}$$

$$Ee_i = k_{\psi air} \cdot \frac{Ra_i}{\lambda} \tag{2}$$

$$k_{\psi air.i} = \left|\frac{\psi_{air.i} - \psi_{air.min}}{\psi_{air.max} - \psi_{air.min}}\right| \tag{3}$$

$$\psi_{air.i} = \frac{R \cdot T}{M_v} \cdot ln\left(\frac{ea}{es}\right) = 0.46191456 \cdot\ T\ \cdot \ln(RH) \tag{4}$$

Where: $ETo_{MJS(\psi air;Ra)}$ – reference evapotranspiration estimated using the Moretti-Jerszurki-Silva model (mm day^{-1}); *a* – linear coefficient of the regression equation derived from the association between "ψ_{air} vs. ETo_{PM}" (mm day^{-1}); *b* – angular coefficient of the regression equation derived from the association between "ψ_{air} vs ETo_{PM}" (dimensionless); Ee_i – equivalent water evaporation on the *i*-th day (mm day^{-1}); $K_{\psi air.i}$ – proportionality coefficient of the atmospheric water potential on the *i*-th day (dimensionless); Ra_i – solar radiation at the top of the atmosphere on the *i*-th day (MJ m^{-2} dia^{-1}), estimated according to ASCE-EWRI (2005); λ – latent heat of water vaporization (2.45 MJ kg^{-1}); $\psi_{air.i}$ – atmospheric water potential on the *i*-th day (MPa); $\psi_{air.max}$ – maximum atmospheric water potential observed during the analyzed period (MPa); $\psi_{air.min}$ – minimum atmospheric water potential observed during the analyzed period (MPa); *R* – universal gas constant (8.314 J mol^{-1} K^{-1}); *T* – average air temperature during the considered period (K); *Mv* – molar mass of water (18 . 10^{-6} m^3 mol^{-1}); *ea* – actual vapor pressure during the considered period (MPa); *es* – saturation vapor pressure during the considered period (MPa); *RH* – relative humidity of the air (dimensionless).

The *MJS* model parameters used (a = –0.0888 mm day^{-1} and b = 0.3683, for $\psi_{air.min}$ = 28.5 MPa and $\psi_{air.max}$ = 156.0 MPa) were calibrated by Silva (2021) with data measured at meteorological stations in the TRB, from the period between Jan/2014 and Dec/2018, using the Least Squares Method to adjust the coefficients.

The spatialization of *Ra* considered the input of the Julian day variables (*J*; days) and local latitude (φ; radians). The values of *J* and φ were spatialized with a processing module created in the QGIS software. The ψ_{air} was generated with temperature (Te_{SR}; °C) and relative humidity (RHe_{SR}; %) images of the air, estimated through remote sensing, which served as input for Equation 4. With $\psi_{air.min}$ and $\psi_{air.max}$ obtained during the study period, $K_{\psi air}$ was estimated using Equation 3. The *Ee* was calculated with the images generated from *Ra* and $K_{\psi air}$, with the Equation 2. Finally, with the specialized *Ee* and the calibrated coefficients *a* and *b* of the *MJS* model, the spatially distributed $ETo_{MJS(\psi air;Ra)}$ was obtained (Equation 1).

In the estimation of $ETo_{MJS(\psi air;Ra)}$, air temperature and relative humidity were used as input, obtained with the multiple linear model (Equations 5 and 6), established by Silva (2021):

$$Te_{RS(Wp;Ts)} = a_2 \cdot Wp\ +\ a_1 \cdot Ts\ +\ a_0 \tag{5}$$

$$RHe_{RS\ (Wp;Ts)} = a_2 \cdot Wp\ -\ a_1 \cdot Ts\ + a_0 \tag{6}$$

Where: $Te_{RS(Wp;Ts)}$ – air temperature estimated with remote sensing by multiple linear adjustment (°C); Wp – total column of precipitable water vapor estimated with the Aqua MODIS satellite, MYD05_L2 product (cm); Ts – land surface temperature estimated from band 10 of the Landsat 8 satellite (°C); $RHe_{RS(Wp;Ts)}$ – relative humidity of the air estimated with remote sensing by multiple linear adjustment (%); a_2, a_1, a_0 – coefficients of the equation obtained from the multiple linear adjustment for temperature (a_2 = 1.75 °C cm^{-1}; a_1 = 0.52, a_0 = 3.25 °C) and relative humidity (a_2 = 1.74 °C cm^{-1}; a_1 = – 0.97, a_0 = 87.85 °C).

The analysis of the spatial variability of $ETo_{MJS(\psi air;Ra)}$ in the TRB (image pixel) was conducted using images representing the seasons of summer (January 4 to February 18), autumn (April 3 to May 26), winter (July 8 to August 21), and spring (October 8 to November 10), under scenarios classified according to the Oceanic Niño Index (ONI) by GGWS (2021). The analyses considered the years: 2013, representing the expected climatological normality for the region; 2015, dominated by El Niño; and 2011, dominated by La Niña. These scenarios aimed to evaluate the spatial variability of ETo under different climatic conditions throughout the seasons of the year.

The satellite images used to estimate and analyze the variation of $ETo_{MJS(\psi air;Ra)}$ in the TRB were grouped by climatic scenario (Table 1), specifying the satellites, orbit/point, and dates corresponding to the seasons of the year.

Table 1 – Acquisition dates of satellite images and sensors used for the analysis of the spatial variability of $ETo_{MJS(\psi air;Ra)}$ in the Tibagi River Basin (TRB), under three climatic scenarios, across the four seasons of the year.

--------- Satellites orbit/point ----------		------------------------ Seasons of the Year --------------------------			
Aqua – MODIS	Landsat – TIRS	Summer	Autumn	Winter	Spring
-- Normal Scenario (Year: 2013) --					
h13v11	221/77	2013-01-10(2)	2013-05-26(1)	2013-07-29(1)	2013-11-10(2)
	221/78	2013-01-10(2)	2013-05-26(1)	2013-07-29(1)	2013-11-10(2)
	222/76	2013-02-18(2)	2013-05-01(1)	2013-08-21(1)	2013-11-09(1)
	222/77	2013-02-18(2)	2013-05-01(1)	2013-08-21(1)	2013-10-08(1)
--- El Niño Scenario (Year: 2015) ---					
h13v11	221/77	2015-01-24(1)	2015-05-16(1)	2015-08-04(1)	2015-10-07(1)
	221/78	2015-02-09(1)	2015-05-16(1)	2015-08-04(1)	2015-10-07(1)
	222/76	2015-01-15(1)	2015-05-07(1)	2015-08-11(1)	2015-10-14(1)
	222/77	2015-01-15(1)	2015-05-07(1)	2015-08-11(1)	2015-10-30(1)
-- La Niña Scenario (Year: 2011) --					
h13v11	221/77	2011-01-29(3)	2011-04-19(3)	2011-07-08(3)	2011-11-05(2)
	221/78	2011-01-29(3)	2011-04-03(3)	2011-07-16(2)	2011-10-28(3)
	222/76	2011-01-04(3)	2011-04-10(3)	2011-07-15(3)	2011-11-04(3)
	222/77	2011-01-04(3)	2011-04-10(3)	2011-07-15(3)	2011-11-04(3)

(1) Images obtained from the Landsat 8 satellite; (2) Images obtained from the Landsat 7 satellite; (3) Images obtained from the Landsat 5 satellite. (Source: The authors)

Each Landsat 8 satellite scene covers an area of 190 km (height) by 180 km (width), while the Aqua satellite, MODIS sensor, captures an area of 2040 km (height) by 2880 km (width). Since the Tibagi River Basin (TRB) is 25000 km^2, four Landsat scenes were required to cover the entire basin, compared to just one Aqua image. The mosaic of Landsat 8 and Aqua MODIS images was created using QGIS software for each season across the evaluated scenarios (Normal, El Niño, and La Niña), resulting in 12 mosaics of the TRB.

The selection of images used for estimating *ETo* considered the following criteria and conditions: *i*) Spatialized *ETo* was estimated for the seasons of summer (December 21 to March 19), autumn (March 20 to June 20), winter (June 21 to September 21), and spring (September 22 to December 20). Spatializing *ETo* by season aimed to mitigate the influence of land use effects from those associated with ENSO, facilitating comparisons; *ii*) Preference was given to images collected in the middle of each season (summer, autumn, winter, and spring) to capture the typical climate of the season; *iii*) Priority was given to clear-sky conditions, with up to 40% cloud cover, in Landsat satellite images; *iv*) For the creation of mosaics of input images for estimating spatialized $ETo_{MJS(\psi air;Ra)}$, a maximum difference of 30 days between images was established; *v*) Preference was given to images collected by Landsat 5 and 8 satellites, and in cases of intense cloud cover, Landsat 7 was used. Landsat 7 images were avoided due to the presence of data gaps (no data values) in pixel rows.

The Landsat 7 images were restored during the resampling process using the "Nearest neighbor method" (Boggione; Fonseca, 2004) to correct rows with missing data, generating interpolated images with improved quality. The QGIS software (Meyer; Riechert, 2019) was used for image correction, following these procedures: *i*) Using the "Convert format" algorithm, pixels with "no data" were assigned a value of zero in the input image. This procedure must be performed on images composed of a single band, as multi-band image compositions are not accepted by the algorithm; *ii*) Subsequently, the "Fill no data" algorithm was applied to estimate the value of "no data" pixels through interpolation of neighboring pixels. The maximum search distance for neighboring pixels was set to 10 pixels.

The estimation of the temporal $ETo_{MJS(\psi air;Ra)}$ values between Landsat 8 satellite images was performed using linear interpolation. Input images with the lowest possible cloud cover percentage from the year of climatic normality (2013) were used, considering the quality of the input data. Only images for orbit/point 222/76 (representing Cfa climate) and orbit/point 221/77 (representing Cfb climate) were used. The effectiveness of the temporal interpolation algorithm "r.series.interp" was tested in areas of 10 km x 10 km in the northern (Cfa climate) and southern (Cfb climate) parts of the TRB (Figure 1). The purpose of the interpolation was to generate synthetic images at a daily frequency for one year of analysis (2013), using only twelve images (one per month).

The interpolation algorithm "r.series.interp" from the Grass7 provider is a processing tool in the QGIS software (Meyer; Riechert, 2019). To configure the algorithm, the required information fields were filled out as follows: *i*) "Input raster layer(s)" – These are the images containing $ETo_{MJS(\psi air;Ra)}$ values generated for the dates available from the satellites. Each file was named to reflect the imaging date; *ii*) "Point position for each input map" – The dates of satellite image acquisition were provided in integer format (without separators), arranged chronologically from the oldest to the most recent image, using the year-month-day format; *iii*) "Name for the output raster map" – The name of the output interpolated image, with each file identified by the interpolated date of interest (the name of each output image must be separated by commas); *iv*) "Sampling point position for each output map" – The date of the interpolated image of interest, provided in integer format (without separators) and arranged chronologically from the oldest to the most recent, according to the year-month-day format (each date must be separated by commas); *v*) "Linear interpolation method": The only method currently supported by the "r.series.interp" algorithm (linear) was tested.

Using the interpolation results, it was possible to generate interpolated *ETo* values with the Moretti-Jerszurki-Silva model ($ETo_{MJS(\psi air;Ra)int}$) for the days between available Landsat images or those with cloud cover above 40%.

The satellite images selected for the region (orbit/point 222/76 and 221/77) were acquired throughout 2013, with one image chosen per month (Table 2), having a maximum cloud cover of 30% to 40%, a criterion that can be indicated at the time of image acquisition. One image was sampled per month so that the input data set closely approximated the regional climatic reality, as well as allowing for the verification of the quality of the results between months.

Table 2 – Sensors and date of acquisition of the satellite images in 2013, used in the analysis of the temporal variability of $ETo_{MJS(\psi air;Ra)int}$, in the Tibagi River Basin (TRB)

Satellites orbit/point		Climate	Months											
Aqua MODIS	Landsat TIRS		Jan.	Feb.	Mar.	Apr.	May	Jun.	Jul.	Aug.	Sep.	Oct.	Nov.	Dec.
			Dias											
h13v11	221/77	Cfb	10(1)	11(1)	31(1)	16(1)	26(2)	11(2)	29(2)	30(2)	07(1)	09(1)	10(1)	04(2)
	222/76	Cfa	01(1)	18(1)	22(1)	23(1)	01(2)	18(2)	04(2)	21(2)	22(2)	08(2)	09(2)	11(2)

(1) Images obtained with Landsat 7 satellite; (2) Images obtained with Landsat 8 satellite. (Source: The authors)

The validation of the *ETo* obtained with the alternative interpolated method (*MJS*; $ETo_{MJS(\psi air;Ra)int}$) was evaluated in association with the *ETo* estimated using the standard Penman-Monteith ASCE method (ETo_{PM}; ASCE-EWRI, 2005). ETo_{PM} estimates were calculated for all the days of the year when daily data were available, for the LDA-IPR and PGA-SIM stations (Table 3). The stations were selected for having fewer divergent points between the observations with the Penman-Monteith ASCE model and *MJS* (Silva, 2021), and for being in distinct climatic conditions.

Table 3 – Identification, location, and characterization of the meteorological stations in the Tibagi River Basin used in the analyses.

Identification	Station	Institute	Latitude	Longitude	Altitude (m)	Climate
LDA-IPR	Londrina	IAPAR	23°13’12,00” S	51°06’00,00” W	585	Cfa
PGA-SIM	Ponta Grossa	SIMEPAR	25°00’49,32”S	50°09’08,64”W	885	Cfb

(Source: The authors).

The Penman-Monteith ASCE model (ASCE-EWRI, 2005) was calculated using daily data measured at the meteorological stations (ETo_{PM}), while the alternative *MJS* model (Equation 1) used spatialized meteorological variables (Te_{RS} e RHe_{RS}) as input.

The statistical analyses of the validation consisted of checking the associations between: “ETo_{PM} estimated with data from the meteorological stations vs. $ETo_{MJS(\psi air;Ra)int}$ interpolated with the r.series.interp algorithm”. The following indicators were used: Nash-Sutcliffe Efficiency Index (*NSE*), Concordance Index "*d*", Root Mean Square Error (*RMSE*), Mean Absolute Percentage Error (*MAPE*), and Pearson Correlation Coefficient (*r*). The significance level of the *r* value was verified using the *t*-test at 99% (**) significance. If this requirement was not met, the test was performed at 95% (*), and if neither criterion was met, the *r* value was considered non-significant (*ns*).

III. RESULTS AND DISCUSSION

Spatial variability of $ETo_{MJS(\psi air;Ra)}$ in the TRB

In the image mosaic of the seasons (Figure 2), the boundaries of the scenes composing the TRB were clearly identified, especially in the images from the autumn of 2013 and 2015, and winter of 2011. However, the images were not homogeneous, as different days had to be used to cover the entire basin in the study, representing the *ETo* of the TRB. The orbits/points 222/76, 222/77 (northern part of the basin), 221/77, and 221/78 (southern part of the basin) do not pass over the same location on the same day. Therefore, the mosaic for the same season of the year was composed of different dates (Table 1).

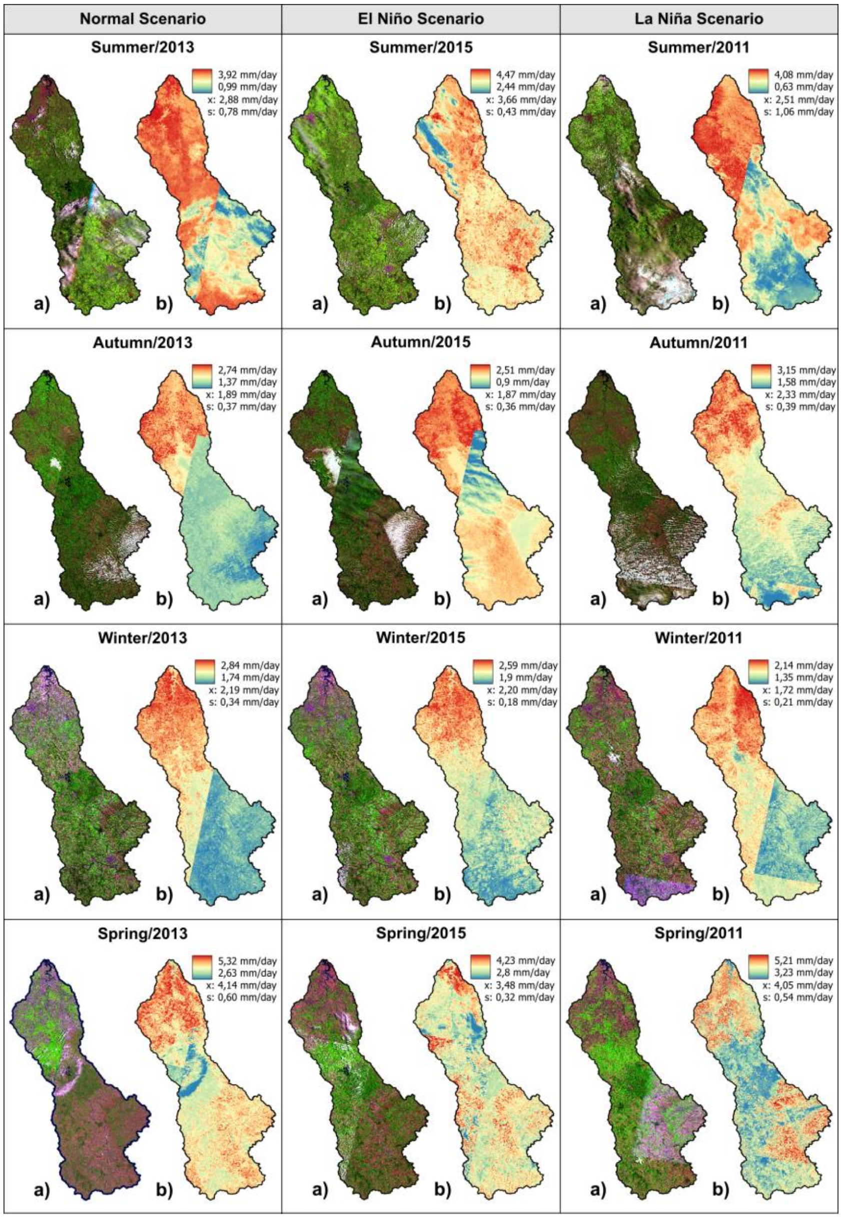

Figure 2 – Spatial variability of $ETo_{MJS(\psi air;Ra)}$ in the Tibagi River Basin (TRB), across the seasons and scenarios: normal (year 2013), El Niño (year 2015), and La Niña (2011), where: a) False color composition for cloud cover visualization; and b) Image with $ETo_{MJS(\psi air;Ra)}$ (mm day^{-1}) values estimated with remote sensing data ("x" is the mean and "s" is the standard deviation of $ETo_{MJS(\psi air;Ra)}$ values in the basin). (Source: The authors).

The difference in average $ETo_{MJS(\psi air;Ra)}$ for the TRB (Figure 2) between the Normal and El Niño scenarios was 0.78 mm day^{-1} in summer, 0.02 mm day^{-1} in autumn, 0.01 mm day^{-1} in winter, and 0.66 mm day^{-1} in spring. Between the Normal and La Niña scenarios, the average difference in $ETo_{MJS(\psi air;Ra)}$ was 0.37, 0.44, 0.47, and 0.09 mm day^{-1} in summer, autumn, winter, and spring, respectively. Considering the smaller average differences between the spatially estimated evapotranspiration values, the Normal scenario during autumn and winter (colder seasons; Figure 2) was similar to the El Niño scenario. In summer and spring (warmer seasons; Figure 2), the Normal scenario was similar to La Niña.

The average ETo_{PM} estimated using data measured at meteorological stations showed no difference within the same season for the climate scenarios (La Niña, Normal, and El Niño), but differences were observed between the analyzed climate types Cfa and Cfb (Figure 2). However, the spatialized average $ETo_{MJS(\psi air;Ra)}$ exhibited differences within the same season across the climate scenarios (Figure 2). The *MJS* model shows high sensitivity to air temperature and relative humidity (Jerszurki et al., 2017), climatic variables that control atmospheric water potential and are used in climate classification systems (Alvares et al., 2013). In this context, *ETo* estimated using the *MJS* model tends to show greater variability across seasons and climate types compared to the Penman-Monteith model.

The average $ETo_{MJS(\psi air;Ra)}$ obtained through remote sensing for the basin was calculated considering all evapotranspiration values estimated across approximately 27,704,045 pixels in the TRB (Figure 2). The confidence interval for the mean $ETo_{MJS(\psi air;Ra)}$ is very narrow and close to the true mean due to the sample size.

The difference in results between ETo_{PM} (estimated using data measured at meteorological stations) and $ETo_{MJS(\psi air;Ra)}$ (estimated using remote data) may be related to the insufficient data series for spatial evapotranspiration estimation with the Penman-Monteith model. In the estimation of spatialized evapotranspiration, the spatial variability and the size of the TRB contributed to highlighting differences between the averages within the same season under different scenarios.

The ETo_{PM} estimated for the Cfa climate (LDA-IPR meteorological station) and Cfb climate (PGA-SIM meteorological station) showed no spatial variation (as the stations did not vary spatially), but temporal variation was observed. Thus, ENSO events (which represent temporal variation) did not influence the variation in ETo_{PM} (measured at the meteorological station location) within the same season or across different years (Figure 2). The use of only one year of observation for each scenario may have contributed to the lack of variation in ETo_{PM} among ENSO events during the same season. Meza (2005), evaluating 23 years of evapotranspiration data in Central Chile, found differences in the variable across seasons, where during autumn and winter, *ETo* in La Niña and Normal periods was similar and higher than in El Niño periods. However, during spring and summer, the Normal period showed higher values than La Niña and El Niño, which had more comparable values.

Therefore, for a more consistent analysis, extending the data series would be necessary to capture greater evapotranspiration variation due to ENSO events. The main challenge for such an analysis is obtaining years with well-characterized ENSO events, complete with satellite imagery and uninterrupted meteorological data series. Studies by Nagel et al. (2020) (review on nanosatellites) and Beck et al. (2023) (high-resolution

ISSN eletrônico 2177-2738
RA'EGA, Curitiba, PR, V.62, n.1, p. 44–66, 4/2025
http://dx.doi.org/10.5380/raega.v62i1.98349

climate data based on observations and projections) suggest that conducting analyses similar to the present study may not be a limitation in the near future, given the increasing availability of free satellite imagery and more representative open-access data series. This will enable easier detection of greater spatial and temporal variation in evapotranspiration.

The largest differences in average ETo_{PM} were observed between Cfa and Cfb climates during winter (0.6 mm day^{-1}) and spring (0.6 mm day^{-1}), as well as the highest average evapotranspiration magnitudes in these climates during summer (4.2 mm day^{-1}) and spring (4.5 mm day^{-1}), and the lowest during autumn (2.7 mm day^{-1}) and winter (2.8 mm day^{-1}) (Figure 2). The same trend (difference and magnitude) in evapotranspiration was observed for the spatialized $ETo_{MJS(\psi air;Ra)}$ in the TRB (Figure 2), with the highest values in the northern part of the basin (Cfa) and the lowest in the southern part (Cfb).

As presented in Figure 2, Matzenauer et al. (2008) observed higher ETo_{PM} values (estimated with the Penman-Monteith model) in spring in Rio Grande do Sul during La Niña events and Normal years, as well as higher ETo_{PM} in winter only during Normal years. The average spatialized $ETo_{MJS(\psi air;Ra)}$ for each scenario in the TRB (Figure 2) was 2.77 mm day^{-1} for the Normal scenario, 2.80 mm day^{-1} for El Niño, and 2.65 mm day^{-1} for La Niña. The results of the present study are aligned with Matzenauer et al. (2008).

The type of land cover is directly related to ETo_{PM}, considering that part of the incident radiation is reflected by the surface (albedo). $ETo_{MJS(\psi air;Ra)}$ is not directly influenced by albedo but indirectly through the effects of radiation, T, and RH, depending on the surface type. Any surface receiving a certain amount of radiation tends to increase its temperature and consequently its emission, according to Stephan-Boltzmann's Law. The orbital sensor on the satellite captures solar energy (electromagnetic radiation) reflected by a surface at a specific wavelength (Meneses; Almeida, 2012). Therefore, bright objects such as exposed soil (magenta tone in Figure 2a) reflect a significant amount of energy, while dark objects such as dense vegetation (dark green tone in Figure 2a) reflect less energy to the sensor.

In the spatialization of $ETo_{MJS(\psi air;Ra)}$, the highest values were observed in areas with exposed soil, and the lowest in more vegetated areas, indicating that evapotranspiration in the TRB was higher when local temperatures were elevated, which is consistent. The results showed that $ETo_{MJS(\psi air;Ra)}$ (estimated with remote sensing data) varied with land use, and the spatialization methodology for evapotranspiration proved promising for estimating atmospheric water demand, considering local conditions, especially in areas without nearby meteorological station data.

During the methodological development, one of the challenges was having to associate different images (Landsat and Aqua) for the execution of some processing modules. For generating the $Te_{RS(Wp;Ts)}$ and $RHe_{RS(Wp;Ts)}$, the file names of the satellite images needed to be organized according to the imaging date, so that the respective daily temperature and relative humidity data could be inserted into the processing module more quickly and efficiently. Landsat provides its files named with the date (year-month-day), but in Aqua/MODIS, the naming is done with the Julian day.

Thus, to perform the associations 'Wp vs. Ts vs. RHm_{MS}' and 'Wp vs. Ts vs. Tm_{MS}', the Wp and Ts variables had to be organized and renamed by their acquisition date. The file organization allowed the generation of spatialized temperature and humidity to be performed for multiple images, with the help of the QGIS processing module. However, the process of renaming the files had to be done image by image, which took time in preparing the data.

The Python script developed to transform the hdf file (Aqua/MODIS) into geotiff (a format accepted by QGIS) allowed only one image of interest to be processed at a time, which made the process of generating the final Wp image slower. The processing modules developed in QGIS greatly helped with the speed of image processing. However, the "Raster Calculator" algorithm, used in almost all modules, could not be used as input data during the workflow. Due to the inefficiency of the algorithm, the methodology had to be divided into several processing modules until the final result of the spatialized $ETo_{MJS(\psi air;Ra)}$ calculation was reached, requiring more processing time.

Automating multiple images at the same time, with just one script to generate the Wp and the module to generate the $ETo_{MJS(\psi air;Ra)}$, would be ideal to speed up the processing. Such a procedure would ensure greater use of the established methodology, which could be made feasible by programming routines in Python (the language in which algorithms are developed within QGIS).

The main difficulty in developing and applying the methodology was the various steps to be carried out, from obtaining the images to processing the remote sensing data, taking months to arrive at the final $ETo_{MJS(\psi air;Ra)}$ calculation for the entire basin. Furthermore, the processing modules underwent several testing stages until they could generate the expected final product. To spread the use of the methodology proposed in this study, one alternative would be to develop an online system in collaboration with the Google Earth Engine platform, similar to the SSEBop-Br algorithm (ANA, 2020), automating the acquisition of images. Such a system would have access to satellite images and meteorological data directly from the source platforms, enabling the

ISSN eletrônico 2177-2738
RA'EGA, Curitiba, PR, V.62, n.1, p. 44–66, 4/2025
http://dx.doi.org/10.5380/raega.v62i1.98349

application of the calculations from the methodology proposed in this work, using the obtained data. Another option would be to develop a program (plugin) executable within QGIS, using the Python language.

The lack of correction for the directional and angular effects of MODIS can lead to differences in the obtained images (Gao et al., 2017), especially in images above 30°. In the present study, no such issues were observed, but the lack of correction could be a limitation for applying the methodology used in areas with higher latitudes. In this case, there are adaptations of the original STARFM algorithm developed by Gao et al. (2006) (Wang et al., 2014), which could still allow for corrections and the use of the methodology proposed and tested in this study. MODIS also provides products corrected by the Bidirectional Reflectance Distribution Function (BRDF), such as MCD43A1 Collection 5 (Che et al., 2017), which correct the images and eliminate the effects of the wide scanning field of the MODIS sensor.

The remote models developed based on the surface energy balance – the High-Resolution Evapotranspiration Mapping Model with Internalized Calibration Model (Metric; Allen et al., 2007); and the Simplified Operational Surface Energy Balance Model (SSEBop; ANA, 2020) – already have a platform that provides ready-to-use evapotranspiration images, indicating the possibility of streamlining the methodology proposed in this study. Silva (2021) evaluated the efficiency of estimating $ETo_{MJS(\psi air;Ra)}$ with the same proposed methodology. The platforms for models like METRIC were developed precisely due to the difficulty of having access to quality meteorological data, specific calibration, and specialized technical personnel for applying the various model equations (Allen et al., 2011).

The advantage of spatially estimated $ETo_{MJS(\psi air;Ra)}$ lies in its possibility to estimate it for locations with limited meteorological information, such as in the North of Brazil (Amazon region) and other areas where the number of stations is lower compared to the southern region of Brazil. Even in the TRB, where evapotranspiration differences are based on land use and land cover, there was consistency in the relationship between radiation balance (Rn) and $ETo_{MJS(\psi air;Ra)}$. Therefore, using spatially estimated values for a specific location may be more advantageous than using the ETo_{PM} value from a station located many kilometers away from the area under study. Alternatively, it can enable the determination of ETo for large areas, such as a river basin.

Spatialized evapotranspiration can have a variety of applications. Paula et al. (2019) obtained promising estimates of actual evapotranspiration using the SSEBop model in the Preto River basin, Federal District, while managing irrigation with center pivots. In the present study, only spatialized reference evapotranspiration was evaluated, but the methodology could also be used to adjust irrigation depth based on $ETo_{MJS(\psi air;Ra)}$.

Temporal variability of $ETo_{MJS(\psi air;Ra)}$

The best satellite images for each month of 2013, with the lowest possible cloud cover, were selected for the Cfa and Cfb climates, as presented in Figure 3, respectively. Following the criteria established for selecting images used as input for temporal interpolation, twelve images from the Cfa climate (Figure 3.I) were employed to estimate daily reference evapotranspiration. In the Cfb climate (Figure 3.II), the images from February (2013, February 11) and June (2013, June 11) were excluded from the analysis due to complete cloud cover over the entire study area during those periods. These data were excluded to avoid being a source of error and inaccuracy in the final estimation results. For both analyzed climates, it was observed that $ETo_{MJS(\psi air;Ra)}$ (Figure 3) values during the summer and spring months were higher than those recorded in autumn and winter in the TRB. This pattern aligns with the spatial analysis results (Figure 2).

Gao et al. (2006) developed an algorithm that combines the qualities of the Landsat satellite (30 m spatial resolution) and the MODIS sensor (daily temporal resolution) aboard the Aqua/Terra satellites. The algorithm, which consists of a Spatial and Temporal Adaptive Reflectance Fusion Model (STARFM) applied to Landsat and MODIS images, requires calibration and atmospheric correction to surface reflectance for the images. This requirement arises from differences in data processing, acquisition time, band width, geolocation errors, and spatial resolution.

The authors highlighted the following factors that complicated the image fusion process: *i*) The non-homogeneous observation of MODIS, as it may include mixed land cover types considering the spatial resolution of Landsat; *ii*) Land cover and pixel geolocation errors can change during the prediction period; and *iii*) Phenological variation in vegetation and solar geometry alter image reflectance between the input and output dates. However, although the algorithm improves spatial resolution by combining Landsat and MODIS data, the fusion may compromise spectral resolution, increasing potential errors related to differences in the spectral characteristics of the sensors and data processing, particularly in heterogeneous areas (Wang et al., 2014).

ISSN eletrônico 2177-2738
RA'EGA, Curitiba, PR, V.62, n.1, p. 44–66, 4/2025
http://dx.doi.org/10.5380/raega.v62i1.98349

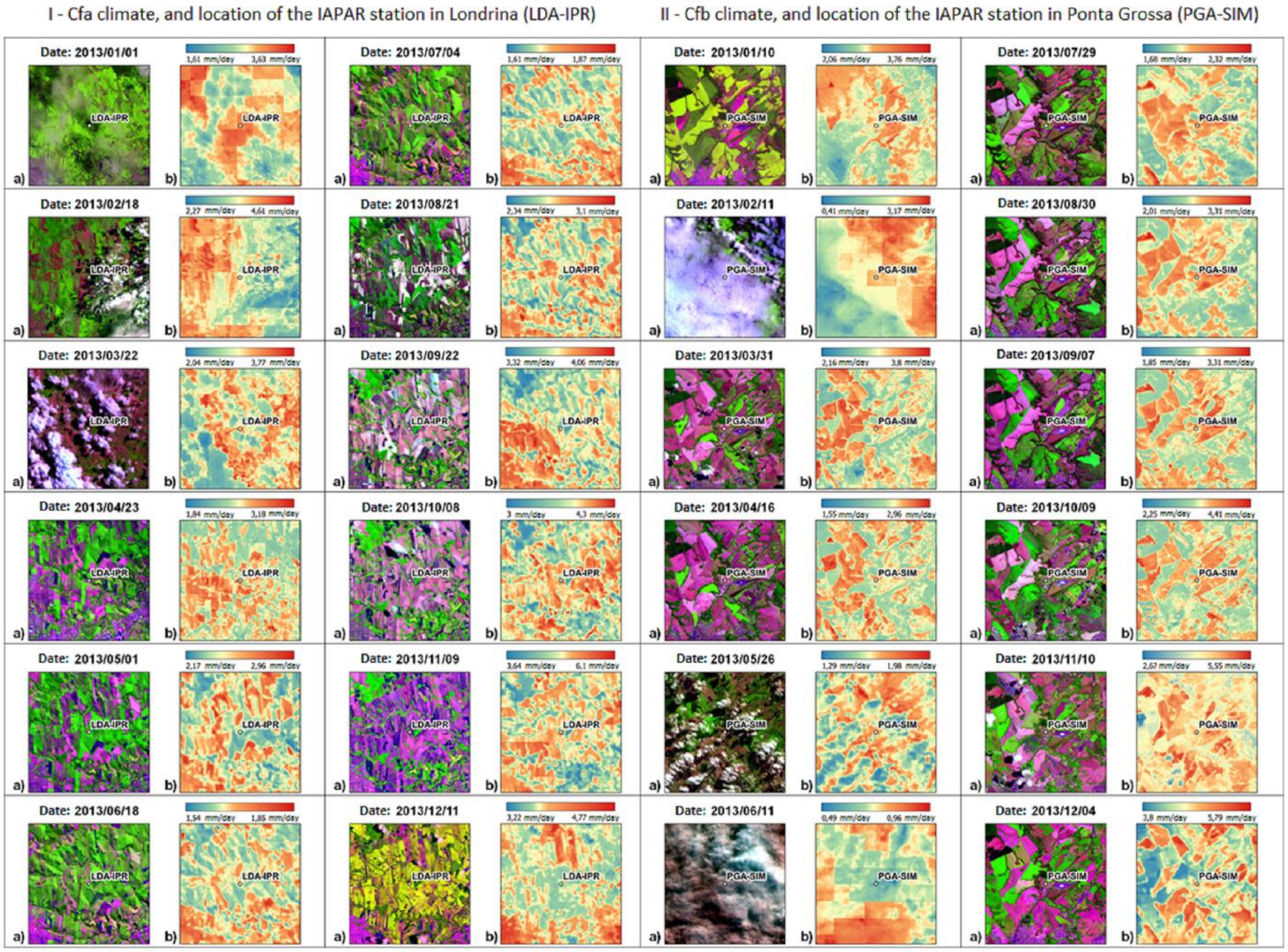

I - Cfa climate, and location of the IAPAR station in Londrina (LDA-IPR)

II - Cfb climate, and location of the IAPAR station in Ponta Grossa (PGA-SIM)

Figure 3 – Best Landsat 7 and 8 satellite images from 2013 (Normal scenario) used to form the input database for temporal interpolation: I) Cfa climate, with the location of the IAPAR weather station in Londrina (LDA-IPR); and II) Cfb climate, with the location of the IAPAR weather station in Ponta Grossa (PGA-SIM). Where: "a" is the false-color composite image for cloud cover visualization; and "b" is the image showing $ETo_{MJS(\psi air;Ra)}$values (mm day^{-1}) estimated using remote sensing data. (Source: The authors).

The issues reported by Gao et al. (2006) and the complexity of executing the STARFM algorithm were the reasons behind the proposal and use of a simplified temporal interpolator in the present study. The "r.series.interp" algorithm in QGIS offers the advantage of being a tool available within a GIS platform that can be used solely with the satellite featuring the best spatial resolution (Landsat) to interpolate the period desired by the user, without requiring numerous transformations to achieve the final product. Furthermore, the literature review did not identify scientific studies testing the efficiency of "r.series.interp." However, the QGIS algorithm provides only the linear interpolation method, which limited its use and the estimation of daily $ETo_{MJS(\psi air;Ra)int}$, failing to adequately track the variation of ETo_{PM} (Figure 4).

The methodology developed to estimate $ETo_{MJS(\psi air;Ra)int}$ using temporally interpolated remote sensing data allowed for obtaining only average values, which were compared to ETo_{PM} (Figure 4.I). Statistically, this resulted in reasonable values for the indicators *RMSE*, *MAPE*, and *r*, but poor values for *NSE* and *d* (Figure 4.II). The lack of sensitivity in the $ETo_{MJS(\psi air;Ra)int}$ estimates, as evidenced by the "vertical alignments" observed in Figure 4.II, indicates that $ETo_{MJS(\psi air;Ra)int}$ did not follow the precise variation of ETo_{PM}. This limitation negatively impacted the *NSE* and *d* indicators, which measure the proximity of association points to the 45^o line (1:1 line).

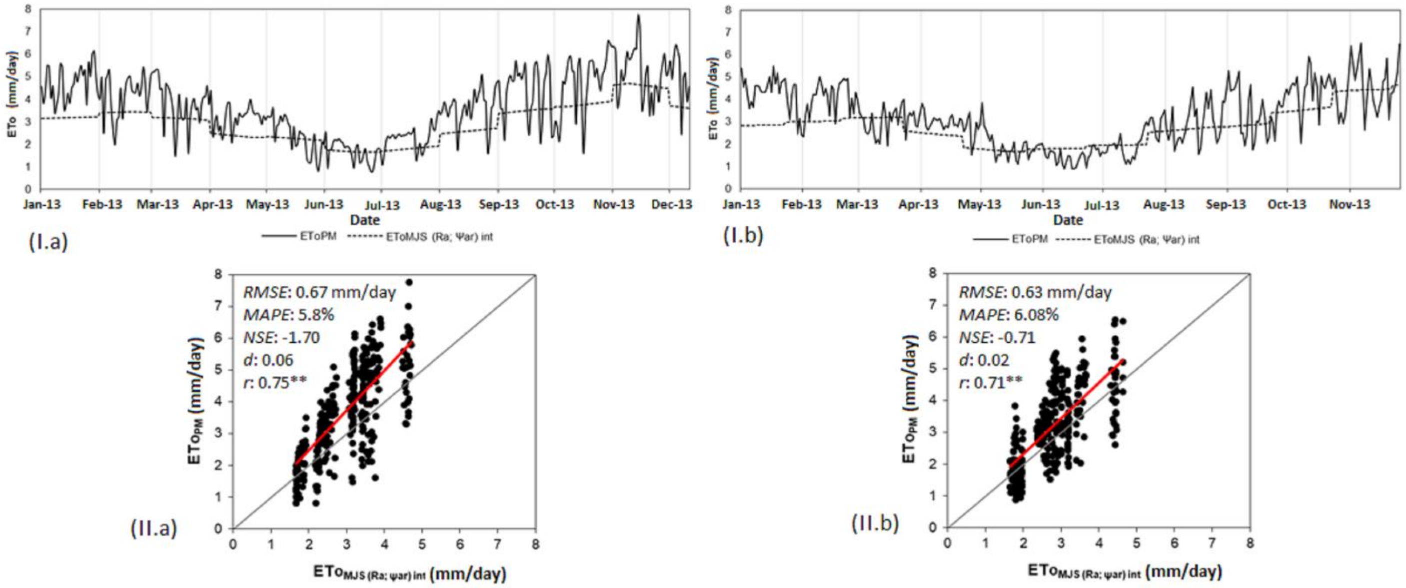

Figure 4 – Reference evapotranspiration calculated using the Penman-Monteith ASCE model (ETo_{PM}; based on station-measured data) and the Moretti-Jerszurki-Silva model ($ETo_{MJS(\psi air;Ra)int}$; based on temporally interpolated remote sensing data): I) Time series; and II) Linear regression analysis and statistical indicators obtained between the respective values "$ETo_{MJS(\psi air;Ra)int}$ vs. ETo_{PM}." Where: "a" refers to the LDA-IPR station, Cfa climate; and "b" refers to the PGA-SIM station, Cfb climate. (Source: The authors).

However, even with perfectly suitable methodologies and models for estimating *ETo*, achieving better *NSE* and *d* indicators would only be possible by determining the most appropriate time frame (before and after a high-resolution scene) for fusing MODIS data. In the present study, the synthetic daily images for 2013 were based on only twelve images (one per month).

The literature shows considerable variation regarding the most appropriate temporal scale for images. Walker et al. (2012), using the STARFM algorithm to evaluate the fusion of Landsat-MODIS data for forest phenology, analyzed MODIS reflectance data with daily, eight-day, and sixteen-day compositions. The authors observed good performance with the eight-day composition but highlighted that it may be unsuitable for phenological changes occurring over shorter time scales. Gao et al. (2017), assessing crop development in the field through image fusion with the STARFM algorithm, pointed out that it is challenging to obtain two clear pairs of Landsat-MODIS images with surface conditions reasonably similar to the target prediction date. For the single-pair option, the automatic system choices include: *i*) selecting the image pair closest to the prediction date; or *ii*) using the image pair with the highest spatial correlation to the MODIS image on the prediction date.

One of the advantages of QGIS software is its ability to create routines using the Python programming language (Rogers; Staub, 2013). Thus, with adequate programming knowledge, it is possible to reproduce the algorithm with interpolation methods more robust than the linear approach. The use of Python is highly beneficial for automating routines, particularly those focused on the use/generation of spatialized data.

Validation of $ETo_{MJS(\psi air;Ra)int}$ estimates

Continuous high-resolution spatial and temporal monitoring of evapotranspiration is essential for improving water resource management, particularly irrigation practices. However, currently available satellites lack mechanisms to integrate high spatial and temporal resolutions within a single sensor (Wang et al., 2019). Due to these limitations, numerous spatial and temporal fusion techniques have been developed to extract the best information from each sensor.

In the literature, numerous studies have shown how high spatial resolution and image acquisition frequency obtained with nanosatellites and CubeSats have improved agricultural management and sustainability (Nagel et al., 2020). However, studies comparing high-resolution satellite data (such as PlanetScope) with broader resolution data (Landsat 8 and Sentinel 2) are still common (Shimizo et al., 2020; Amankulova et al., 2023; Ibrahim; Balzter, 2024). Despite the lower resolution of satellites in larger constellations, data integration can improve the accuracy of estimates by correcting variations in variables such as surface temperature and vegetation fraction. Nagel et al. (2020) noted that the costs of images from nanosatellites and CubeSats (PlanetScope and Doves) limit their use, particularly in long-term research. The authors added that, due to the superior quality of sensors, open-source data provided by national space agency satellites will continue to be popular.

Landsat and MODIS satellites are the most commonly used platforms for data fusion. The main reasons are: Landsat has moderately high spatial resolution and MODIS has daily temporal resolution (Yang et al., 2016; Januar et al., 2020); and, the images are free, and the available archive is large enough for temporal studies. The easy access to Landsat and MODIS images allows public agencies to improve water resource management in large areas, such as river basins, at a low cost.

The use of MODIS data for daily *ETo* estimation has been studied for several years. Paredes et al. (2021), estimating daily *ETo* with remote sensing data from the geostationary satellite Meteosat Second Generation (available to European countries), achieved excellent results ($r > 0.98$ and $RMSE = 0.13$ mm day^{-1}). The limitation of evapotranspiration data spatialized with the MODIS sensor and the Meteosat satellite is the spatial resolution, around 1 km and 4 km, respectively. The low spatial resolution limits the use of evapotranspiration on a local scale. Higher resolutions can provide detailed information on water use in crops and soil moisture status, allowing for optimized irrigation efficiency in small farms (Ke et al., 2017).

Many studies are being developed trying to combine MODIS and Landsat data (Cammalleri et al., 2014; Li et al., 2017; Yi et al., 2018) with the aim of estimating daily *ETo* images with 30 m resolution. However, most of the studies developed have some difficulty in reproducing the methodology. Given the complexity found in existing methodologies, the present work proposed testing the quality of the temporal interpolation algorithm of the QGIS software, which used only Landsat images to perform the temporal estimation.

The temporal variation of ETo_{PM} for the Cfa and Cfb climate types was greater than the estimation of $ETo_{MJS(\psi air;Ra)int}$ (Figure 4.I “a” and “b”), using the temporal interpolator tested in the present study. The evapotranspiration estimated with the Penman-Monteith method (ETo_{PM}) has the advantage of non-linearly combining the main variables (temperature, relative humidity, radiation, and wind speed) that influence the process, in addition to being based on the input of variables measured every day. On the other hand, it is considered that the temporal estimation of $ETo_{MJS(\psi air;Ra)int}$ with only 12 and 10 images for the Cfa and Cfb climates, respectively, is a relatively small sample to feed the temporal interpolator to generate daily evapotranspiration values throughout the year.

It is important to emphasize that the interpolator function of the “r.series.interp” algorithm is linear (the only one available), which explains the existence of linearity between one month and another (Figure 4.I “a” and “b”). Thus, even before performing the analyses, it was expected that the algorithm would not be able to represent the variability of ETo_{PM}, due to the simplicity of the interpolation. However, these tools are rapidly developing, and if the algorithm provides more robust interpolators (polynomial), the performance in the estimates could be significantly improved, as the temporal trend of ETo_{PM} has a follows a sinusoidal pattern.

Even using a linear interpolator, the trend of the interpolated evapotranspiration ($ETo_{MJS(\psi air;Ra)int}$) was similar to ETo_{PM} (Figure 4.I “a” and “b”), which indicated an extremely interesting result for use in activities aimed at planning large areas with limited meteorological data available. Moreover, with the trend of technological advancement, in the near future it will be possible to obtain satellite images with high temporal and spatial resolution, all on a single platform, offering details with shorter revisit times for the same reference point. A shorter period between satellite images would allow for better estimates of $ETo_{MJS(\psi air;Ra)int}$, more accurately following the trend and variability of ETo_{PM}. Furthermore, greater detail would enable local and watershed-scale studies with higher precision in the spatial analysis of $ETo_{MJS(\psi air;Ra)int}$.

Li et al. (2017), using the STARFM algorithm, fused data from the MODIS sensor (daily temporal resolution) and the ASTER satellite (90 m spatial resolution) to obtain daily remote sensing data. The information was used as input to estimate spatialized ETo (with the Surface Energy Balance System – SEBS model), which, when compared to ETo measured with local equipment, resulted in temporal estimates with $RMSE$ = 0.88 mm day^{-1}. Yi et al. (2018), using the same methodology, obtained $RMSE$ = 0.80 mm day^{-1} and $MAPE$ = 13.40%. Cammalleri et al. (2014), using the same algorithm with MODIS and Landsat data, achieved $RMSE$ = 1.32 mm day^{-1} and $MAPE$ = 24.95%.

Compared to the literature, the results found in the present study (Figure 4.II "a" and "b") with the indicators r, $RMSE$, and $MAPE$ showed better performance. However, NSE and d indicated worse performance in the temporal estimation. Therefore, it is considered that $ETo_{MJS(\psi air;Ra)int}$ can only be estimated with acceptable precision. The values of $ETo_{MJS(\psi air;Ra)int}$ generally followed the ETo_{PM} trend, but the distance or amplitude of the point values can be quite discrepant (Figure 4).

IV. CONCLUSIONS

Spatialized evapotranspiration allowed identifying differences within the same season across the analyzed climatic scenarios.

The methodology developed to estimate spatialized $ETo_{MJS(\psi air;Ra)}$ over large areas has acceptable statistical precision, but the process of creating the final mosaic for large coverage areas, such as the TRB, still proved to be labor-intensive. The temporal estimation of evapotranspiration has satisfactory statistical precision ($RMSE$ = 0.65 mm day^{-1}; r = 0.73; $MAPE$ = 5.94%; NSE = –1.2; d = 0.04). The number of viable images and the linear interpolation algorithm limited the possibility of obtaining daily ETo_{PM} variations over time.

V. REFERENCES

ALLEN, R. G.; TASUMI, M.; TREZZA, R. Satellite-Based Energy Balance for Mapping Evapotranspiration with Internalized Calibration METRIC – Model. Journal of Irrigation and Drainage Engineering, Asce, v. 133, n. 4, p. 380-394, 2007.

ALLEN, R.; IRMAK, A.; TREZZA, R.; HENDRICKX, J. M. H.; BASTIAANSSEN, W.; KJAERSGAARD, J. Satellite-based ET estimation in agriculture using SEBAL and METRIC. Hydrological Processes, v. 25, n. 26, p. 4011-4027, 2011. Wiley. http://dx.doi.org/10.1002/hyp.8408.

ALVARES, C. A.; STAPE, J. L.; SENTELHAS, P.; GONÇALVES, J. L. M.; SPAROVEK, G. Köppen's climate classification map for Brazil. Meteorologische Zeitschrift, v. 22, n. 6, p. 711-728, 2013. Schweizerbart. http://dx.doi.org/10.1127/0941-2948/2013/0507.

AMANKULOVA, K.; FARMONOV, N.; AKRAMOVA, P.; TURSUNOV, I; MUCSI, L. Comparison of PlanetScope, Sentinel-2, and landsat 8 data in soybean yield estimation within-field variability with random forest regression. Heliyon, v. 9, e17432, 2023. https://doi.org/10.1016/j.heliyon.2023.e17432

ANA (Agência Nacional de Águas). Estimativas de evapotranspiração real por sensoriamento remoto no Brasil. 4. ed. Brasília: Ana, 2020. 23 p.

ASCE-EWRI (New York). American Society of Civil Engineers. The ASCE Standardized Reference Evapotranspiration Equation. New York: American Society of Civil Engineers, 2005. 70 p. Task Committee Report.

BECK, H. E.; McVICAR, T. R.; VERGOPOLAN, N.; BERG, A.; LUTSKO, N. J.; DUFOUR, A.; ZENG, Z.; JIANG, X.; VAN DIJK, A. I. J. M.; MIRALLES, D. G. High-resolution (1 km) Köppen-Geiger maps for 1901–2099 based on constrained CMIP6 projections. Scientific Data, v. 10, n. 724, 2023. https://doi.org/10.1038/s41597-023-02549-6

BOGGIONE, G. A.; FONSECA, L. M. G. Restoration of Landsat-7 Images. National Institute For Space Research, São José dos Campos, 2004. Disponível em: <http://mtc-m12.sid.inpe.br/rep/sid.inpe.br/jeferson/2004/01.13.13.12>.

CAMMALLERI, C.; ANDERSON, M. C.; GAO, F.; HAIN, C. R.; KUSTAS, W. P. A data fusion approach for mapping daily evapotranspiration at field scale. Water Resources Research, v. 49, n. 8, p. 4672-4686, 2013. American Geophysical Union (AGU). http://dx.doi.org/10.1002/wrcr.20349.

CAMMALLERI, C.; ANDERSON, M. C.; GAO, F.; HAIN, C. R.; KUSTAS, W. P. Mapping daily evapotranspiration at field scales over rainfed and irrigated agricultural areas using remote sensing data fusion. Agricultural and Forest Meteorology, v. 186, p. 1-11, 2014. Elsevier BV. http://dx.doi.org/10.1016/j.agrformet.2013.11.001.

CAVALCANTI, I. F. A.; CARRIL, A. F.; PENALBA, O. C.; GRIMM, A. M.; MENÉNDEZ, C. G.; SANCHEZ, E.; CHERCHI, A.; SÖRENSSON, A.; ROBLEDO, F.; RIVERA, J. Precipitation extremes over La Plata Basin – Review and new results from observations and climate simulations. Journal of Hydrology, v. 523, p. 211-230, 2015. Elsevier BV. http://dx.doi.org/10.1016/j.jhydrol.2015.01.028.

CHE, X.; FENG, M.; SEXTON, J. O.; CHANNAN, S.; YANG, Y.; SUN, Q. Assessment of MODIS BRDF/Albedo Model Parameters (MCD43A1 Collection 6) for Directional Reflectance Retrieval. Remote Sensing, v. 9, n. 1123, 2017. https://doi.org/10.3390/rs9111123

GAO, F.; ANDERSON, M.; ZHANG, X.; YANG, Z.; ALFIERI, J. G.; KUSTAS, W. P.; MUELLER, R.; JOHNSON, D. M.; PRUEGER, J. H. Toward mapping crop progress at field scales through fusion of Landsat and MODIS imagery. Remote Sensing of Environment, v. 188, p. 9–25, 2017. http://dx.doi.org/10.1016/j.rse.2016.11.004.

GAO, F.; MASEK, J.; SCHWALLER, M.; HALL, F. On the blending of the Landsat and MODIS surface reflectance: predicting daily landsat surface reflectance. Transactions on Geoscience and Remote Sensing, [S.L.], v. 44, n. 8, p. 2207-2218, 2006. Institute of Electrical and Electronics Engineers (IEEE). http://dx.doi.org/10.1109/tgrs.2006.872081.

GGWS (Golden Gate Weather Services). El Niño and La Niña Years and Intensities. 2021. Disponível em: https://ggweather.com/enso/oni.htm. Acesso em: 22 maio 2021.

IBRAHIM, S.; BALZTER, H. Evaluating flood damage to paddy rice fields using PlanetScope and Sentinel-1 data in north-western Nigeria: Towards potential climate adaptation strategies. Remote Sensing, v. 16, n. 3657, 2024. https://doi.org/10.3390/rs16193657

JANUAR, T. W.; LIN, T.; HUANG, C.; CHANG, K. Modifying an Image Fusion Approach for High Spatiotemporal LST Retrieval in Surface Dryness and Evapotranspiration Estimations. Remote Sensing, v. 12, n. 3, p. 498, 2020. MDPI AG. http://dx.doi.org/10.3390/rs12030498.

JERSZURKI, D.; SOUZA, J. L. M.; SILVA, L. C. R. Expanding the geography of evapotranspiration: an improved method to quantify land-to-air water fluxes in tropical and subtropical regions. PLOS ONE, v. 12, n. 6, p. 1-20, 2017. Public Library of Science (PLOS). http://dx.doi.org/10.1371/journal.pone.0180055.

KE, Y. I. M, J.; PARK, S.; GONG, H. Spatiotemporal downscaling approaches for monitoring 8-day 30 m actual evapotranspiration. Isprs Journal of Photogrammetry and Remote Sensing, v. 126, p. 79-93, 2017. Elsevier BV. http://dx.doi.org/10.1016/j.isprsjprs.2017.02.006.

LI, Y.; HUANG, C.; HOU, J.; GU, J.; ZHU, G.; LI, X. Mapping daily evapotranspiration based on spatiotemporal fusion of ASTER and MODIS images over irrigated agricultural areas in the Heihe River Basin, Northwest China. Agricultural and Forest Meteorology, v. 244-245, p. 82-97, 2017. Elsevier BV. http://dx.doi.org/10.1016/j.agrformet.2017.05.023.

MATZENAUER, R.; BERLATO, M. A.; SAMPAIO, M. R.; TRINDADE, J. K. Efeitos do fenômeno Enos sobre a evapotranspiração de referência na região do Planalto Médio do Rio Grande do Sul, Brasil. Pesq. Agrop. Gaúcha, v. 14, n. 1, p. 67-70, 2008.

MENESES, P. R.; ALMEIDA, T. Introdução ao processamento de imagens de sensoriamento remoto. Bahia: Cnpq, 2012. 276 p.

MEYER, D.; RIECHERT, M. Open source QGIS toolkit for the Advanced Research WRF modelling system. Environmental Modelling & Software, v. 112, p. 166-178, 2019. Elsevier BV. http://dx.doi.org/10.1016/j.envsoft.2018.10.018.

MEZA, F. J. Variability of reference evapotranspiration and water demands. Association to ENSO in the Maipo river basin, Chile. Global and Planetary Change, v. 47, n. 2-4, p. 212-220, 2005. Elsevier BV. http://dx.doi.org/10.1016/j.gloplacha.2004.10.013.

NAGEL, G. W.; NOVO, E. M. L. M.; KAMPEL, M. Nanosatellites applied to optical Earth observation: a review. Ambiente e Água, v. 15, n. 3, e2513, 2020. https://doi.org/10.4136/ambi-agua.2513

PAREDES, P.; TRIGO, I.; BRUIN, H.; SIMÕES, N.; PEREIRA, L. S. Daily grass reference evapotranspiration with Meteosat Second Generation shortwave radiation and reference ET products. Agricultural Water Management, v. 248, p. 106543, 2021. Elsevier BV. http://dx.doi.org/10.1016/j.agwat.2020.106543.

PAULA, A. C. P.; SILVA, C. L.; RODRIGUES, L. N.; SCHERER-WARREN, M. Performance of the SSEBop model in the estimation of the actual evapotranspiration of soybean and bean crops. Pesquisa Agropecuária Brasileira, v. 54, p. 1-11, 2019. FapUNIFESP (SCIELO). http://dx.doi.org/10.1590/s1678-3921.pab2019.v54.00739.

ROGERS, S. R; STAUB, B. Standard use of Geographic Information System (GIS) techniques in honey bee research. Journal of Apicultural Research, v. 52, n. 4, p. 1-48, 2013. Informa UK Limited. http://dx.doi.org/10.3896/ibra.1.52.4.08.

ROSA, S. L. K.; SOUZA, J. L. M.; SANTOS, A. A. Data from NASA Power and surface weather stations under different climates on reference evapotranspiration estimation. Pesquisa Agropecuária Brasileira, v. 58; e03261, 2023. https://doi.org/10.1590/s1678-3921.pab2023.v58.03261

ISSN eletrônico 2177-2738
RA'EGA, Curitiba, PR, V.62, n.1, p. 44–66, 4/2025
http://dx.doi.org/10.5380/raega.v62i1.98349

SHIMIZO, K.; OTA, T.; MIZOUE, N.; SAITO, H. Comparison of multi-temporal PlanetScope data with Landsat 8 and Sentinel-2 data for estimating airborne LiDAR derived canopy height in temperate forests. Remote Sensing, v. 12, n. 1876, 2020. https://doi.org/10.3390/rs12111876.

SILVA, D. P. Associação espaço-temporal de variáveis meteorológicas com técnicas de sensoriamento remoto para estimativa da evapotranspiração. Curitiba, 2021. 173p. Dissertação (Mestrado em Agronomia, área de concentração Ciência do Solo) – Setor de Ciências Agrárias, Universidade Federal do Paraná. Disponível em: https://acervodigital.ufpr.br/handle/1884/74849 Acesso em: 02 agosto 2024

TALSMA, C. J.; GOOD, S. P.; JIMENEZ, C.; MARTENS, B.; FISHER, J. B.; MIRALLES, D. G.; MCCABE, M. F.; PURDY, A. J. Partitioning of evapotranspiration in remote sensing-based models. Agricultural and Forest Meteorology, v. 260-261, p. 131-143, 2018. Elsevier BV. http://dx.doi.org/10.1016/j.agrformet.2018.05.010.

WALKER, J. J.; BEURS, K. M.; WYNNE, R. H.; GAO, F. Evaluation of Landsat and MODIS data fusion products for analysis of dryland forest phenology. Remote Sensing of Environment, v. 117, p. 381-393, 2012.

WANG, P.; GAO, F.; MASEK, J. G. Operational data fusion framework for building frequent Landsat-like imagery. IEEE Transactions on Geoscience and Remote Sensing, v. 52, n. 11, 2014. http://dx.doi.org/10.1109/TGRS.2014.2311445

WANG, T.; TANG, R.; LI, Z.; JIANG, Y.; LIU, M.; NIU, L. An Improved Spatio-Temporal Adaptive Data Fusion Algorithm for Evapotranspiration Mapping. Remote Sensing, v. 11, n. 7, p. 761, 2019. MDPI AG. http://dx.doi.org/10.3390/rs11070761.

YANG, G.; WENG, Q.; PU, R.; GAO, F.; SUN, C.; LI, H.; ZHAO, C. Evaluation of ASTER-Like Daily Land Surface Temperature by Fusing ASTER and MODIS Data during the HiWATER-MUSOEXE. Remote Sensing, v. 8, n. 1, p. 75, 2016. MDPI AG. http://dx.doi.org/10.3390/rs8010075.

YI, Z.; ZHAO, H.; JIANG, Y. Continuous Daily Evapotranspiration Estimation at the Field-Scale over Heterogeneous Agricultural Areas by Fusing ASTER and MODIS Data. Remote Sensing, v. 10, n. 11, p. 1694, 2018. MDPI AG. http://dx.doi.org/10.3390/rs10111694.

ZHU, X.; CHEN, J.; GAO, F.; CHEN, X.; MASEK, J. G. An enhanced spatial and temporal adaptive reflectance fusion model for complex heterogeneous regions. Remote Sensing of Environment, v. 114, n. 11, p. 2610-2623, 2010. Elsevier BV. http://dx.doi.org/10.1016/j.rse.2010.05.032.